

Parallel Fabrication of Plasmonic Nanocone Sensing Arrays

Andreas Horrer, Christian Schäfer, Katharina Broch, Dominik A. Gollmer, Jan Rogalski, Julia Fulmes, Dai Zhang, Alfred J. Meixner, Frank Schreiber, Dieter P. Kern, and Monika Fleischer*

A fully parallel approach for the fabrication of arrays of metallic nanocones and triangular nanopyramids is presented. Different processes utilizing nanosphere lithography for the creation of etch masks are developed. Monolayers of spheres are reduced in size and directly used as masks, or mono- and double layers are employed as templates for the deposition of aluminum oxide masks. The masks are transferred into an underlying gold or silver layer by argon ion milling, which leads to nanocones or nanopyramids with very sharp tips. Near the tips the enhancement of an external electromagnetic field is particularly strong. This fact is confirmed by numerical simulations and by luminescence imaging in a confocal microscope. Such localized strong fields can amongst others be utilized for high-resolution, high-sensitivity spectroscopy and sensing of molecules near the tip. Arrays of such plasmonic nanostructures thus constitute controllable platforms for surface-enhanced Raman spectroscopy. A thin film of pentacene molecules is evaporated onto both nanocone and nanopyramid substrates, and the observed Raman enhancement is evaluated.

1. Introduction

Sensing platforms with sensitivities down to the level of a few molecules and high chemical specificity play a major role in medicine, biology, and environmental or safety monitoring. Plasmonic nanostructures are under intense investigation as the basic elements for optical sensors, the functionality of which is based on localized surface plasmon polaritons.^[1] Strongly enhanced local near-fields can be employed for high

sensitivity sensing of analytes in thin films, fluidic or gaseous test volumes by employing surface-enhanced Raman spectroscopy (SERS).^[2] Apart from rough metal films or assemblies of colloidal particles, arrangements of top-down fabricated metallic nanostructures in a variety of well-defined shapes have been prepared to focus light down to sub-diffraction limited volumes with local high near-field enhancement.^[3] Metallic nanocones present an advantageous geometry for sensing that has been explored very little so far due to their nontrivial fabrication. Sharp cone tips lead to well-defined highly localized areas of excitation and high field intensity. They are well accessible for analyte molecules or for selective functionalization. By fabricating cones with a defined height and aspect ratio, their plasmon resonance frequency can be pre-determined according to the application. Accordingly, nanocones present an attractive geometry for applications such as plasmonic photovoltaics, nanoscale point light sources, or near-field microscopy.^[4] Recently, some strategies for metallic nanocone fabrication were presented.^[5] The authors established a method using metallization, local deposition of etch masks, and subsequent ion milling to obtain regular arrays of smooth metallic cones.^[6] Compared to other

A. Horrer, C. Schäfer, K. Broch, D. A. Gollmer, J. Fulmes, Prof. F. Schreiber, Prof. D. P. Kern, Prof. M. Fleischer
Institute for Applied Physics and Center LISA^[+]
Eberhard Karls Universität Tübingen
Auf der Morgenstelle 10, 72076 Tübingen, Germany
E-mail: monika.fleischer@uni-tuebingen.de



J. Rogalski, Dr. D. Zhang, Prof. A. J. Meixner
Institute of Physical and Theoretical Chemistry and Center LISA^[+]
Eberhard Karls Universität Tübingen
Auf der Morgenstelle 15, 72076 Tübingen, Germany

DOI: 10.1002/sml.201300449

methods, these cones exhibit very sharp tips, while the procedure enables good control over size and shape. The process however is semi-serial, which limits the possibilities of large-scale fabrication for applications such as sensing platforms.

One general approach for parallel nanostructure fabrication is nanosphere lithography (NSL).^[7] Under suitable conditions monodisperse colloidal polystyrene spheres assemble into hexagonally close-packed mono- or bilayers over large areas with good crystal order. Examples of plasmonic structures created by NSL include honeycomb arrays of nanotriangles or nanoparticles, bow-ties, discs, nanocrescents, and nanorings.^[8] Metal cones made by NSL, hole etching, and subsequent evaporation were exemplarily shown.^[5c,d]

Here, a different scheme for the parallel fabrication of extended ordered arrays of nanocones based on NSL is introduced. The principle follows the general fabrication scheme previously established by the authors.^[6] In this case, however, the etch masks are created in a parallel fashion using NSL. Two different modes of application are pursued in this work. In the first case, nanospheres are modified such that they can directly be employed as a well-ordered etch mask. In the second case, single or double layers of nanospheres are used as templates for the evaporation of an etch mask on the underlying metal layer. Either process leads to ordered arrays of sharp-tipped metal cones or triangular pyramids. Their three-dimensional shape distinguishes the present structures from the planar structures typically obtained by NSL.^[9] The process is largely independent of the chosen metal, provided that the mask height is adapted to the respective etch rate. The suitability of the cone arrays as near-field sensing platforms is shown in optical experiments. Local field enhancement by the tips is confirmed by photoluminescence scans in a confocal microscope. Strong Raman intensity enhancement is demonstrated by example of a few monolayers thin film of pentacene.

2. Results

The process for the fabrication of gold nanocones or nanopyramids consists of four major steps, which are shown in **Figure 1**. A substrate is metallized (Figure 1A) and spin-coated with a suspension of polystyrene beads (Figure 1B and the

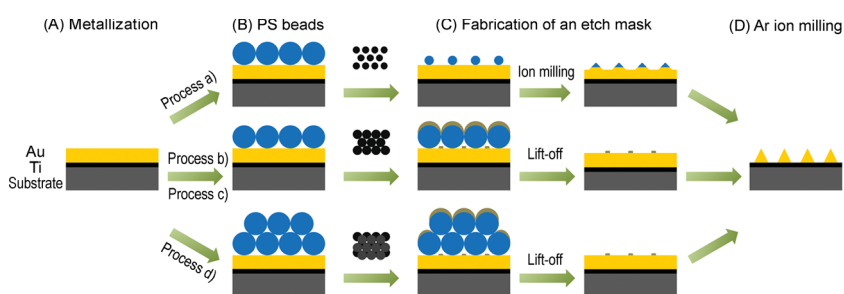


Figure 1. Processing steps for the fabrication of gold nanocones and triangular nanopyramids: A) deposition of Ti and Au; B) spin-coating with a monolayer (processes (a–c)) or double layer (process (d)) of polystyrene beads and thermal post-treatment for process (c); C) fabrication of the etch mask by size reduction in an oxygen plasma (process (a)) or deposition of aluminum oxide and removal of the beads (processes (b–d)); D) argon ion milling under perpendicular incidence, rotating the substrate to correct for potential beam misalignment while forming cones (processes (a, c, d)) or pyramids (process (b)).

Experimental Section). The spin parameters greatly affect the formation of mono- or double layers. While high rotation speeds lead to non-close-packed areas on the sample, decreasing the rotation speed favors the formation of close-packed monolayers. Still lower rotation speeds lead to increasing fractions of double- and multi-layers. Examples of resulting mono- and double layers are shown in **Figure 2a1,b1,d1**.

Next, four different possibilities for obtaining arrays of rotationally symmetric etch masks for the subsequent argon ion milling step are introduced. While processes (a–c) require a close-packed monolayer of beads, process (d) uses a double layer (Figure 1C).

For process (a), the size of the beads is reduced by reactive ion etching with an oxygen plasma. In Figure 2a2 500 nm diameter beads are shown after 110 s of etching. The lateral diameter decreased to about 200 nm, the height to about 170 nm. The beads form a hexagonally ordered array, where the center-to-center-distance equals the original diameter of the beads.

In processes (b), (c), and (d) the beads act as shadow masks for the deposition of a thin aluminum oxide (alumina, Al_2O_3) layer. For processes (b) and (c), a monolayer of spheres is used. The gaps between the beads in process (b) are roughly triangular. The triangles (without their concave corners) have a perpendicular bisector of $(\sqrt{3} - 3/2)d$ (116 nm for $d = 500$ nm), leading to Al_2O_3 masks of roughly the same size and shape (Figure 2b1,b2).^[9] Alternatively, the interstices can be tailored from the triangular to an approximately circular shape with a diameter of only ≈ 40 nm by annealing the spheres at 115 °C on a hotplate before deposition, as shown in process (c) (Figure 2c1).^[10] Deposition of aluminum oxide in this case leads to small circular masks (Figure 2c2). The resulting aluminum oxide masks in processes (b) and (c) form honeycomb patterns where the center-to-center distance of the honeycombs is defined by the sphere diameter d , and the center-to-center distance between neighboring masks by $d/\sqrt{3} \approx 290$ nm (Figure 2b2,c2). The shadow mask for process (d), a double layer, is shown in Figure 2d1. The gaps here appear in a hexagonally ordered pattern and have a hexagonal shape with a distance between two parallel sides of $(2/\sqrt{3} - 1)d$ (80 nm for $d = 500$ nm). This leads to a hexagonally ordered array of aluminum oxide masks of near-circular shape with a spacing of d , see Figure 2d2. In processes (b) to (d), the beads are removed by ultrasonication in toluene.

In the last step, ion milling with an argon ion beam is applied at perpendicular incidence while rotating the substrate (Figure 1(D)). By rotating, tilting of the cone axes due to potential misalignment of the beam is avoided. Characteristically for this process, nanostructures with slanting side-walls form below the mask.^[6] The soft polystyrene bead mask in process (a) is simultaneously etched horizontally and vertically and changes to polystyrene cones with a base angle of about 45° during etching (Figure 2a3). This structure is transferred into the gold layer, resulting in gold cones with the same base angle. Figure 2a4,a5 show an array of cones and

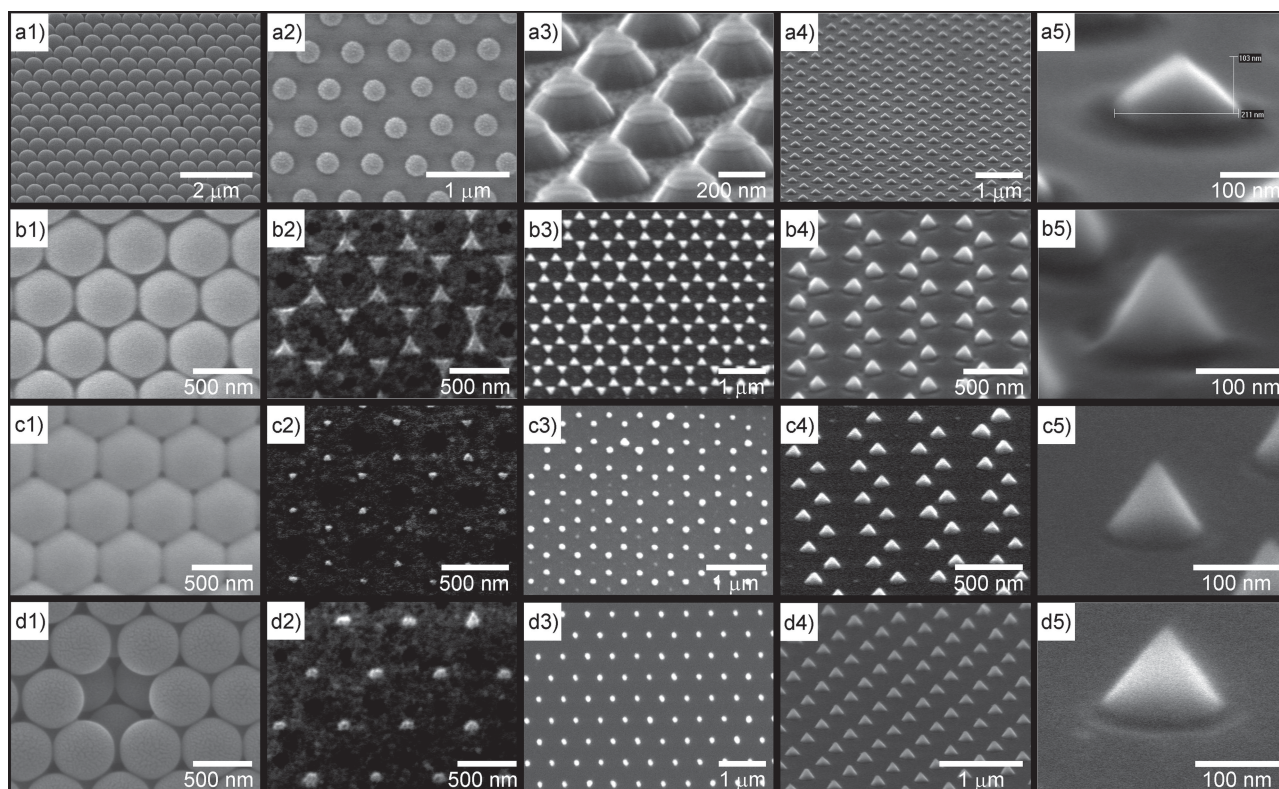


Figure 2. SEM images after each fabrication step: a1,b1,c1) monolayers and d1) double layer of polystyrene beads; a2) polystyrene beads after shrinking; b2,c2,d2) aluminum oxide etch masks; a3) truncated cone with residual polystyrene etch mask; arrays of b3) triangular nanopyramids and c3,d3) nanocones in top view; a4,c4,d4) arrays of nanocones and b4) nanopyramids; a5) single nanocone (base diameter 200 nm, height 100 nm, tip radius < 10 nm), c5,d5) single nanocones (base angle 55°, height 100 nm) and b5) nanopyramid (height 100 nm) fabricated with the four different processes (viewing angle 70°).

a single cone fabricated with process (a). The thickness of the aluminum oxide etch mask in processes (b–d) is chosen such that the mask is completely removed at the same time as the unprotected metal layer. Figure 2b4,b5 show the honeycomb patterns and a single triangular pyramid characteristic of transferring the triangular masks of process (b) into the metal. The circular masks in process (c) correspondingly lead to honeycomb patterns of nanocones (Figure 2c4,c5). In Figure 2d4,d5, the hexagonally ordered array and single cone resulting from process (d) are demonstrated. The cones formed in processes (c) and (d) have base angles of 55° and an aspect ratio of 0.7.

With these methods, large regular arrays of reproducible nanocones and nanopyramids with sharp tips can be fabricated, as exemplarily shown in **Figure 3a**. An area with side lengths of more than 100 μm is homogeneously patterned with hexagonally ordered gold cones, interrupted by occasional grain boundaries and defects. The cones were fabricated according to process (a), using a monolayer of oxygen-treated polystyrene spheres as the mask. Although in this work no wafer-scale patterning was attempted, it was shown by other groups that mostly densely packed nanosphere monolayers can be obtained over several cm².^[11] The fast and cost-efficient process allows for a choice of different metals and arrays with variable densities. As an example, an array of silver nanocones fabricated by process (d) can be seen in Figure 3b. The silver cones exhibit sharp tips as well,

while the tip angle is decreased due to the material dependent milling process.^[6c] The silver cones can be subsequently passivated by a thin layer of Al₂O₃ to avoid corrosion.

A hexagonally ordered array of cones fabricated according to process (d) is investigated in a confocal microscope based on a parabolic mirror (see the Experimental Section). The hexagonal order of the cones is clearly reflected in the photoluminescence pattern in **Figure 4**. The luminescence observed at the cone positions indicates strong field enhancement at the cone tips.

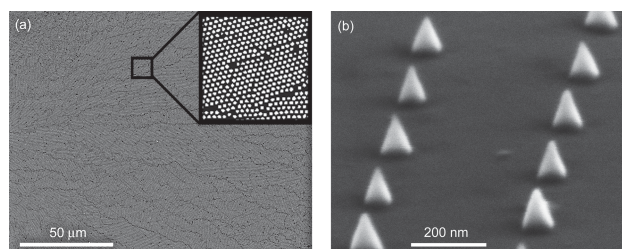


Figure 3. a) SEM overview image of gold nanocones fabricated over an area of more than (100 μm)². Here, polystyrene spheres with their diameters reduced in an oxygen plasma were used as the mask (process (a)). A homogeneous hexagonal pattern of cones with individual grain boundaries and missing cones is formed (see magnified inset). b) Process (d) (double layer and alumina mask) applied to a silver layer leads to sharp-tipped silver cones with a smaller tip opening angle than for the gold cones.^[6c]

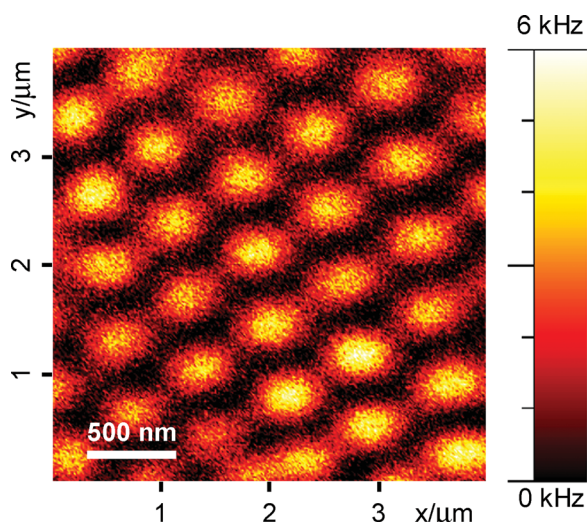


Figure 4. Photoluminescence image of a hexagonal array of gold nanocones obtained by scanning the sample through the focus of a confocal microscope ($\lambda_{\text{ex}} = 632.8$ nm, laser power 270 μW).

SERS provides one means of high sensitivity optical sensing. Depending on the local electric near-field enhancement by the substrate, Raman intensity enhancement of many orders of magnitude can be observed.^[2] To evaluate their Raman intensity enhancement by means of a model system, five distinct surfaces are covered with a thin film of pentacene ($\text{C}_{22}\text{H}_{14}$) molecules.^[12] The different surfaces are: 1) a planar silicon surface, 2) a sputtered rough gold film (thickness 100 nm), 3) hexagonally ordered gold cones with center-to-center distances of 200 nm (process (a)), 4) honeycomb arrays of triangular gold pyramids with center-to-center distances of 290 nm (process (b)), and 5) hexagonally ordered gold cones with center-to-center distances of 500 nm (process (d)). The cones and pyramids are 100 nm high.

The characteristic Raman fingerprint of pentacene molecules consists in peaks located around 1140–1190 cm^{-1} and 1340–1390 cm^{-1} . In **Figure 5**, typical Raman spectra measured on Si, Au, Au cones (500 nm spacing), Au cones (200 nm spacing), and Au pyramids are summarized. The spectra are each averaged over measurements at several different positions.

3. Discussion

The maximum intensity of the peak at 1370 cm^{-1} after background correction is evaluated for the respective spectra. Normalization to the pentacene peak measured on pure silicon shows an overall Raman intensity enhancement factor EF of 1 for silicon, ≈ 90 on gold, ≈ 80 on Au cones (500 nm), ≈ 200 on Au cones (200 nm), and ≈ 130 on triangular Au pyramids. For other prominent Raman peaks, the ratios of the peak heights for the different surfaces is comparable to the ratios for the 1370 cm^{-1} peak, while the signal measured on the Si surface becomes too small to serve as a reference. The increase with denser arrays reflects the fact that more field enhancing structures are present within the focus. Already at 500 nm spacing, the cones almost match the overall enhancement by the full gold layer,

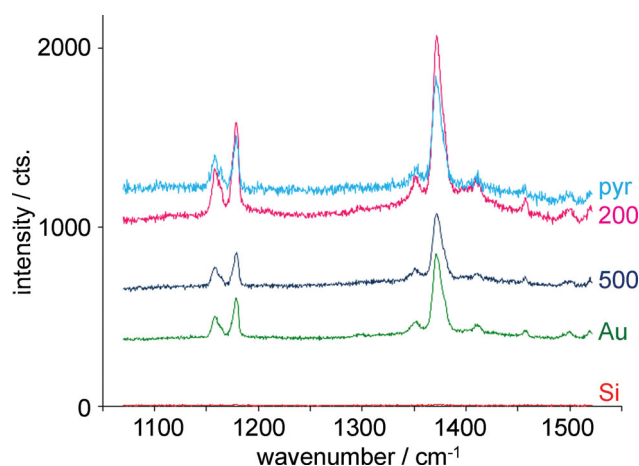


Figure 5. Raman spectra and gold luminescence background of few pentacene layers on silicon (red line) and rough gold substrates (green) compared to hexagonally ordered cones with 500 nm (blue) and 200 nm spacing (magenta), and triangular pyramids in a honeycomb pattern (cyan). The spectra are averaged over several measurements each ($\lambda_{\text{ex}} = 532$ nm, laser power ≈ 5 mW, integration time: 20 s).

while exceeding it for denser arrays. Considering the exposed surface of the structures, the gold area in the focus corresponds to about 13% (500 nm), 80% (200 nm), and 17% (pyramids) of a continuous smooth gold film, respectively. As a very rough estimate for the effective local enhancement factors EF_{eff} of the substrates, the observed overall field enhancement in the focus area A_{foc} is set into relation with the respective active area fractions A_{eff} at which high near-field enhancement takes place. For the nanostructures, this is assumed to correspond to the area covered by cone/pyramid tips A_{tip} , which for the cones were both calculated and observed to dominate the effect of field enhancement,^[6a,13] especially since the fabrication process leads to otherwise smooth surfaces. The signal enhancement observed for one single cone in the focus is very sensitive to the positioning of the focus relative to the cone. **Figure 6** illustrates the distribution of the electric field components in the focus of a linearly polarized laser beam with a wavelength of 532 nm. As shown in Figure 6e,f, if the cones are centered within the focus, mostly the cone base is excited by the horizontal field components (Figure 6b), while the cone tip is most efficiently excited when the cones are positioned slightly off-center within the lobes of vertically oriented electric field (Figure 6d).^[14] The strongest enhancement takes place when the cone is excited by electric field components oriented parallel to the cone axis.^[13] According to the simulations, the maximum tip enhancement exceeds the maximum base enhancement by a factor of ≈ 1.8 and thus dominates the Raman signal (which is roughly proportional to the fourth power of the enhancement factor) by about an order of magnitude. An average number of $N = 4$ cones (500 nm arrays), $N = 23$ cones (200 nm arrays), and $N = 7$ pyramids can be found in a focal spot of 1 μm diameter. According to scanning electron microscope (SEM) images, the tips exhibit radii of around 5–10 nm. This corresponds to an active area on the order of $A_{\text{tip}} \approx 10^{-16}$ m^2 per tip, where the lateral extension of the near-field spot is taken to be on the order of the tip diameter.^[6a] Estimating the effective enhancement per tip according to $EF_{\text{eff}} \approx EF * A_{\text{foc}}/A_{\text{eff}} = EF * A_{\text{foc}}/(N * A_{\text{tip}})$

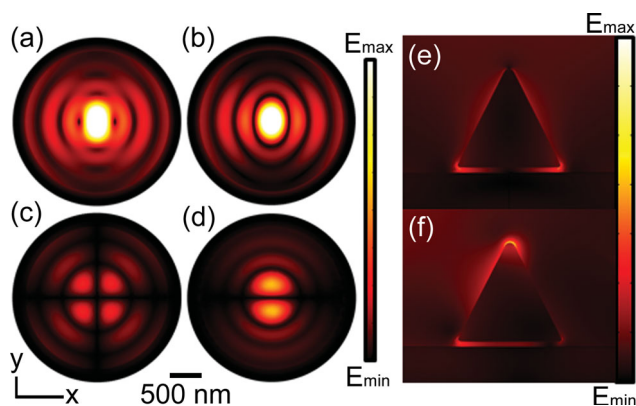


Figure 6. a–d) Numerical simulations of the distribution of the modulus of the electric field in the focus of a 532 nm laser beam with an electric field of 1 V m^{-1} (simulated by waves converging from a hemispherical surface with the electric field on the surface defined as the boundary condition) that is linearly polarized along the y-direction, and e, f) near-field distributions around a cone calculated with COMSOL Multiphysics. a) $|E|$ in the focus, b) $|E_y|$ leading to in-plane excitation, c) weak contribution $|E_x|$, d) $|E_z|$ leading to tip excitation. e) In-plane excitation of the base when the cone is centered in the bright spot (b), f) tip excitation when the cone is positioned slightly off-centered in the bright spots (d). The cone is placed on a silicon surface with a tiny air gap for numerical reasons. The confocal spot diameter is $\approx 1 \mu\text{m}$. The maximum electric near-field at the tip is a factor of ≈ 1.8 stronger than the maximum near-field at the rim of the base, thus dominating the Raman signal by about a factor of 10.

roughly leads to a factor EF_{eff} of 1 for Si and 10^2 for Au if $A_{\text{eff}} = A_{\text{foc}}$ is assumed, since the focus area is fully covered with the respective material. More realistically, EF_{eff} for the rough gold surface depends on many hotspots, whose area coverage and distribution remain largely unknown,^[15] thus adding another factor to the estimate. The rough estimate for EF_{eff} of the nanostructured tips yields a consistent factor of $\approx 10^5$ for the cones spaced at 500 nm, the cones spaced at 200 nm, and the triangular pyramids (compared to pentacene on Si). In view of the above-mentioned sensitivity of the enhancement with respect to the position in the focus, it may well be that not all structures contribute equally, which would further increase EF_{eff} for the structures that do contribute. Although the enhancement factors do not reach current record values, the strength of these surfaces lies in the excellent spatial and spectral control over well-defined narrow hot-spots that are easily accessible for functionalization or selective read-out. It is to be expected that the enhancement factors for the nanostructures can be increased further by applying laser modes with a higher selectivity for the out-of-plane component of the electric field in the focus (e.g., radially polarized light), and optimizing the plasmon resonance of the cones with respect to the excitation wavelength and analyte.

4. Conclusion

In summary, metallic nanocones and triangular nanopyramids present well-defined plasmonic nanostructures with properties attractive for sensing applications. A cost- and time-effective, fully parallel approach for their large-scale

fabrication is established by applying self-assembled nanosphere lithography on metallic thin films and subsequent ion milling. Well-ordered arrays of local masks are created by using the spheres either directly as etch masks, or as a template for etch mask evaporation. Gold cone arrays are demonstrated to display high near-field enhancement factors near the tips, making them promising controllable SERS platforms. Raman enhancement by different nanocone and nanopyramid distributions was evaluated by investigating the intensity of the Raman signal from a thin film of pentacene molecules. The overall enhancement factor for dense arrays clearly surpasses that of a sputtered gold film, with strong Raman enhancement localized at the cone tips.

5. Experimental Section

Nanosphere Lithography: Clean silicon wafers or cover glass slides are used as the substrate. A thin titanium adhesion layer and a gold layer are deposited by e-beam evaporation and resistive heating or sputtering, respectively. The thickness of the gold layer determines the height of the cones or pyramids. 500 nm (carboxyle modified) and 200 nm diameter polystyrene beads are purchased from Polysciences Inc. The concentration of the 2.5% aqueous suspensions is increased to about 10% by controlled evaporation. The metalized substrate is treated with oxygen plasma, which renders the surface hydrophilic to promote the assembly of homogeneous layers of beads. In a first step, fast spinning controls the amount of suspension on the sample. Then the water is evaporated while rotating at lower speed, leaving an ordered layer of beads on the surface. The spin parameters depend on the size of the substrate, the amount of suspension, and the concentration of the beads (e.g., 3000 rpm: 1 s, 1500 rpm: 60 s for a monolayer and 3000 rpm: 1 s, 1000 rpm: 60 s for a large fraction of double layer using a $5 \times 5 \text{ mm}^2$ sample and 5 μL of 10% suspension). When beads are directly used as the etch mask as in Figure 2a2, an oxygen plasma (gas flow 100 sccm, rf power 50 W) is applied to reduce the bead size.^[16] In the reactive ion etching process, the bead height decreases roughly linearly, and the vertical etch rate is determined to about 4 nm s^{-1} . The lateral diameter is reduced at a lower rate while the ions only have access from the exposed top, and reaches a constant rate ($\approx 4 \text{ nm s}^{-1}$) once access from all sides is enabled. The lateral decrease of the diameter can be fitted by an approximate formula.^[16a,c] The aluminum oxide masks are deposited by electron beam physical vapor deposition (with a rate of 0.2 nm s^{-1} at a pressure of $\approx 1.5 \times 10^{-5} \text{ mbar}$). Taking into account the different etch rates, typically a mask thickness of 27 nm is required per 100 nm gold thickness. Since the nanosphere diameter needs to be bigger than the final cone diameter to obtain separated cones, the ratio between the height of the narrow constriction and the mask thickness is at least 2.6:1 for cones with an aspect ratio of 0.7, which should suffice for lift-off. The 200 and 500 nm diameter spheres used for 100 nm high cones in this work (ratio $\geq 3.7:1$) were successfully lifted off in toluene.

Photoluminescence Measurement: The photoluminescence is imaged in a confocal microscope using a 632.8 nm He-Ne laser. The microscope is based on a parabolic mirror for focusing and collection.^[17] The laser beam is radially polarized to generate in the focus of the parabolic mirror an electric field distribution predominantly oriented perpendicular to the sample surface. This mode is

efficient in exciting the vertically oriented transition dipole of the gold cones.^[13] The central spot of the focus has a full width at half maximum of ≈ 260 nm, which is sufficient to resolve the individual cones spaced at 500 nm. The localized surface plasmon resonance of the cone in combination with the lightning rod effect due to the tip leads to a strong electrical near-field enhancement near the tip apex, resulting in local intensive gold luminescence emission from the cone tip.^[13] The sample is scanned through the focus of the parabolic mirror, while the optical signal collected from the surface after filtering the laser line is registered by an avalanche photo diode.

Raman Spectra: Thin films of pentacene molecules are grown with a final average film thickness of 4 nm (growth rate 1 \AA min^{-1}) using organic molecular beam deposition in a UHV-chamber (base pressure 2×10^{-10} mbar). Under these conditions, the first pentacene layers typically exhibit layer-by-layer growth, where the long axis is mostly oriented vertical to the substrate on SiO_x and parallel to the substrate on gold films.^[18] The film thickness thus corresponds to about 2–3 monolayers of upright-standing pentacene molecules (length 1.6 nm).

Note that pentacene is unlikely to strongly chemisorb on the gold, since even aromatic ring systems with oxygen functionalities typically do not exhibit strong chemisorption,^[19] implying that the adsorption is not expected to excessively distort the pentacene molecules in the present case. The Raman spectra are measured using a spectrometer with a confocal microscope (Horiba Jobin Yvon LabRAM HR), a focused linearly polarized Gaussian beam (Torus 50 mW diode pumped solid state laser, excitation wavelength $\lambda_{\text{ex}} = 532$ nm, focus diameter $\approx 1 \text{ \mu m}$, $100\times$ objective with $\text{NA} = 0.9$) and a CCD detector cooled with liquid nitrogen.

Acknowledgements

M.F. would like to thank A. Weber-Bargioni and A. M. Schwartzberg for fruitful discussions. Financial support by the Baden-Württemberg Stiftung is gratefully acknowledged. This project is supported by the European Social Fund and by the Ministry Of Science, Research and the Arts Baden-Württemberg. K.B. gratefully acknowledges support from the Studienstiftung des Deutschen Volkes, and J.F. support from the Carl Zeiss Stiftung. A.J.M. and D.Z. would like to thank the Deutsche Forschungsgemeinschaft through grants ME 1600/5-2 and SPP 1391. J.R. would like to thank the Promotionerverbund "Kohlenstoff auf Substraten: Vom Molekül zur Schicht" according to the Landesgraduiertenförderungsgesetz (LGFG).

- [1] J. N. Anker, W. P. Hall, O. Lyandres, N. C. Shah, J. Zhao, R. P. Van Duyne, *Nat. Mater.* **2008**, *7*, 442.
 [2] M. Moskovits, *J. Raman Spectrosc.* **2005**, *36*, 485.
 [3] M. Fan, G. F. S. Andrade, A. G. Brolo, *Anal. Chim. Acta* **2011**, *693*, 7.
 [4] a) C. Schäfer, D. A. Gollmer, A. Horrer, J. Fulmes, A. Weber-Bargioni, S. Cabrini, P. J. Schuck, D. P. Kern, M. Fleischer, *Nanoscale* **2013**, doi:10.1039/C3NR01292A; b) M. Fleischer, A. Weber-Bargioni, M. V. P. Altoe, A. M. Schwartzberg, P. J. Schuck, S. Cabrini, D. P. Kern, *ACS Nano* **2011**, *5*, 2570.
 [5] a) T. I. Kim, J. H. Kim, S. J. Son, S. M. Seo, *Nanotechnology* **2008**, *19*, 295302; b) J. M. Kontio, H. Husu, J. Simonen, M. J. Huttunen, J. Tommila, M. Pessa, M. Kauranen, *Opt. Lett.* **2009**, *34*, 1979;

- c) H. Fredriksson, Y. Alaverdyan, A. Dmitriev, C. Langhammer, D. S. Sutherland, M. Zäch, B. Kasemo, *Adv. Mater.* **2007**, *19*, 4297; d) L. Isa, K. Kumar, M. Müller, J. Grolig, M. Textor, E. Reimhult, *ACS Nano* **2010**, *4*, 5665.
 [6] a) F. Stade, A. Heeren, M. Fleischer, D. P. Kern, *Microelectron. Eng.* **2007**, *84*, 1589; b) M. Fleischer, F. Stade, A. Heeren, M. Häffner, K. Braun, C. Stanciu, R. Ehlich, J. K. H. Hörber, A. J. Meixner, D. P. Kern, *Microelectron. Eng.* **2009**, *86*, 1219; c) M. Fleischer, D. Zhang, K. Braun, S. Jäger, R. Ehlich, M. Häffner, C. Stanciu, J. K. H. Hörber, A. J. Meixner, D. P. Kern, *Nanotechnology* **2010**, *21*, 065301; d) M. Fleischer, A. Weber-Bargioni, S. Cabrini, D. P. Kern, *Microelectron. Eng.* **2011**, *88*, 2247.
 [7] a) U. C. Fischer, H. P. Zingsheim, *J. Vac. Sci. Technol.* **1981**, *19*, 881; b) H. W. Deckman, J. H. Dunsuir, *Appl. Phys. Lett.* **1982**, *41*, 377; c) J. C. Hultheen, R. P. Van Duyne, *J. Vac. Sci. Technol. A* **1995**, *13*, 1553.
 [8] a) A. J. Haes, C. L. Haynes, A. D. McFarland, G. C. Schatz, R. R. Van Duyne, S. L. Zou, *MRS Bull.* **2005**, *30*, 368; b) J. Merlein, M. Kahl, A. Zuschlag, A. Sell, A. Halm, J. Boneberg, P. Leiderer, A. Leitenstorfer, R. Bratschitsch, *Nat. Photonics* **2008**, *2*, 230; c) C. Langhammer, Z. Yuan, I. Zorić, B. Kasemo, *Nano Lett.* **2006**, *6*, 833; d) Y. Lu, G. L. Liu, J. Kim, Y. X. Mejia, L. P. Lee, *Nano Lett.* **2005**, *5*, 119; e) J. Aizpurua, P. Hanarp, D. S. Sutherland, M. Kall, G. W. Bryant, F. J. Garcia de Abajo, *Phys. Rev. Lett.* **2003**, *90*, 057401.
 [9] C. L. Haynes, R. P. Van Duyne, *J. Phys. Chem. B* **2001**, *105*, 5599.
 [10] A. Kosiorek, W. Kandulski, H. Glaczynska, M. Giersig, *Small* **2005**, *1*, 439.
 [11] a) H. Li, N. Wu, *Nanotechnology* **2008**, *19*, 275301; b) Y. J. Zhang, W. Li, K. J. Chen, *J. Alloys Compd.* **2008**, *450*, 512; c) M. J. K. Klein, M. Guillaumée, B. Wenger, L. A. Dunbar, J. Brugger, H. Heinzelmann, R. Pugin, *Nanotechnology* **2010**, *21*, 205301; d) N. Vogel, L. de Viguerie, U. Jonas, C. K. Weiss, K. Landfester, *Adv. Funct. Mater.* **2011**, *21*, 3064.
 [12] S. Kowarik, K. Broch, A. Hinderhofer, A. Schwartzberg, J. O. Ossó, D. Kilcoyne, F. Schreiber, S. R. Leone, *J. Phys. Chem. C* **2010**, *114*, 13061.
 [13] M. Fleischer, C. Stanciu, F. Stade, J. Stadler, K. Braun, A. Heeren, M. Häffner, D. P. Kern, A. J. Meixner, *Appl. Phys. Lett.* **2008**, *93*, 111114.
 [14] M. A. Lieb, A. J. Meixner, *Opt. Express* **2001**, *8*, 458.
 [15] M. Sackrow, C. Stanciu, M. A. Lieb, A. J. Meixner, *ChemPhysChem* **2008**, *9*, 316.
 [16] a) C. Haginoya, M. Ishibashi, K. Koike, *Appl. Phys. Lett.* **1997**, *71*, 2934; b) P. Hanarp, D. S. Sutherland, J. Gold, B. Kasemo, *Colloid Surf. A* **2003**, *214*, 23; c) A. Horrer, Diplomarbeit, Eberhard Karls Universität Tübingen **2011**.
 [17] D. Zhang, X. Wang, K. Braun, H.-J. Egelhaaf, M. Fleischer, L. Hennemann, H. Hintz, C. Stanciu, C. J. Brabec, D. P. Kern, A. J. Meixner, *J. Raman Spectrosc.* **2009**, *40*, 1371.
 [18] a) C. B. France, P. G. Schroeder, B. A. Parkinson, *Nano Lett.* **2002**, *2*, 693; b) A. Hinderhofer, U. Heinemeyer, A. Gerlach, S. Kowarik, R. M. J. Jacobs, Y. Sakamoto, T. Suzuki, F. Schreiber, *J. Chem. Phys.* **2007**, *127*, 194705; c) S. Kowarik, A. Gerlach, W. Leitenberger, J. Hu, G. Witte, C. Wöll, U. Pietsch, F. Schreiber, *Thin Solid Films* **2007**, *515*, 5606; d) A. C. Dürr, N. Koch, M. Kelsch, A. Rühm, J. Ghijssen, R. L. Johnson, J.-J. Pireaux, J. Schwartz, F. Schreiber, H. Dosch, A. Kahn, *Phys. Rev. B* **2003**, *68*, 115428; e) D. Zhang, U. Heinemeyer, C. Stanciu, M. Sackrow, K. Braun, L. E. Hennemann, X. Wang, R. Scholz, F. Schreiber, A. J. Meixner, *Phys. Rev. Lett.* **2010**, *104*, 056601; F. Schreiber, *Phys. Status Solidi A* **2004**, *201*, 1037.
 [19] a) S. Duhm, A. Gerlach, I. Salzmänn, B. Bröcker, R. L. Johnson, F. Schreiber, N. Koch, *Org. Electron.* **2008**, *9*, 111; b) G. Heime, S. Duhm, I. Salzmänn, A. Gerlach, A. Strozecka, J. Niederhausen, C. Bürker, T. Hosokai, I. Fernandez-Torrente, G. Schulze, S. Winkler, A. Wilke, R. Schlesinger, J. Frisch, B. Bröcker, A. Vollmer, B. Detlefs, J. Pflaum, S. Kera, K. J. Franke, N. Ueno, J. I. Pascual, F. Schreiber, N. Koch, *Nat. Chem.* **2013**, *5*, 189.

Received: February 11, 2013
 Published online: July 12, 2013